

RECONSTRUCTIONNET: A NEURAL NETWORK ARCHITECTURE FOR UNCERTAINTY-AWARE PREDICTIONS WITH EXPLAINABILITY

Anonymous authors

Paper under double-blind review

ABSTRACT

Uncertainty estimation quantifies a model’s confidence in its predictions, fostering calibrated trust among users. Existing approaches face two key limitations: (1) most capture only a single type of uncertainty, and (2) they incur additional training or inference overhead. We propose ReconstructionNet, a neural network that addresses these limitations by modeling the joint input–output distribution with class-specific autoencoders. This enables simultaneous prediction and estimation of both aleatoric and distributional uncertainty in a single pass. Across five real-world datasets, ReconstructionNet matches or surpasses baseline classifiers while producing uncertainty estimates with greater reliability, selectivity, robustness to false negatives, and strong out-of-distribution detection. Furthermore, ReconstructionNet’s architecture naturally supports uncertainty explanations, revealing how individual features contribute to prediction uncertainty without extra computation. Experiments demonstrate that these explanations highlight misclassified regions consistent with human intuition. Together, these contributions establish ReconstructionNet as a unified framework for trustworthy and interpretable artificial intelligence.

1 INTRODUCTION

Uncertainty estimation refers to the task of quantifying how uncertain a machine learning model is about its prediction for each instance. Reliable uncertainty estimates foster calibrated trust by alerting users to cases where the model is likely to be uncertain and erroneous (Toh et al., 2025). Common methods for uncertainty estimation include Bayesian Neural Networks (BNNs) (Jospin et al., 2022), Monte Carlo Dropout (Gal & Ghahramani, 2016) and Deep Ensemble (Lakshminarayanan et al., 2017). These methods quantify one or more of three main types of uncertainty (Malinin & Gales, 2018): 1) Aleatoric (data), 2) Epistemic (model), and 3) Distributional uncertainty. While existing work in uncertainty estimation shows promise, it often faces several limitations. Most uncertainty estimates quantify only a single type of uncertainty and are unable to differentiate between various sources of uncertainty. Furthermore, many uncertainty estimation methods incur increased training and inference time.

We introduce **ReconstructionNet**, a neural network architecture designed to address the aforementioned limitations. ReconstructionNet quantifies aleatoric and distributional uncertainty by modeling the joint input–output distribution with class-specific autoencoders, effectively measuring the distance of an instance from the training data of each class. This design reduces epistemic uncertainty by constraining the state space and allows ReconstructionNet to distinguish between aleatoric and distributional uncertainty.

Beyond identifying when a model is uncertain, understanding which features contribute to prediction uncertainty is equally valuable, giving rise to the emerging field of uncertainty explanation (Wang et al., 2025; Antorán et al., 2021; Fan, 2025). Uncertainty explanations are typically represented as vectors of real values, where each value quantifies the significance and impact of an input feature on the model’s uncertainty. State-of-the-art methods include applying out-of-the-box eXplainable Artificial Intelligence (XAI) techniques, such as Integrated Gradients (IG) (Sundararajan et al., 2017), to explain existing uncertainty estimates (Mougan & Nielsen, 2023; Iversen et al., 2024). Other

approaches involve observing how input perturbations affect prediction uncertainty (Antorán et al., 2021; Wang et al., 2025) and learning which features significantly reduce uncertainty. However, these methods require extra modules on top of uncertainty estimation, increasing inference time.

ReconstructionNet’s design enables inbuilt uncertainty explanation: each class-specific autoencoder produces feature-wise reconstruction errors scaled by learned error weights for classification. Those weighed reconstruction errors quantify each feature’s contribution to the uncertainty, providing uncertainty explanations without additional modules or computation.

The contributions of this research are as follows:

1. Propose ReconstructionNet, a neural architecture that minimises epistemic uncertainty while quantifying and explaining both aleatoric and distributional uncertainty.
2. Provide a theoretical evaluation of ReconstructionNet’s uncertainty explanations.
3. Demonstrate the efficacy of ReconstructionNet for prediction, uncertainty estimation, and explanation on real-world applications in healthcare and finance.

2 RELATED WORK

2.1 UNCERTAINTY ESTIMATION

Definition 1 (Uncertainty Estimation) *For instance $\mathbf{x} \in \mathbb{R}^d$ and a model f , an uncertainty estimator $\sigma(\mathbf{x}; f) : \mathbb{R}^d \rightarrow \mathbb{R}$ assigns a real-valued measure of the prediction uncertainty for \mathbf{x} .*

Uncertainty estimates generally aim to quantify three types of uncertainty:

1. **Aleatoric:** Uncertainty arising from inherent noise in the training data. In classification problems, this manifests as overlapping classes.
2. **Epistemic:** Uncertainty from inadequate model parameter fit, reducible by expanding the dataset or narrowing the hypothesis space.
3. **Distributional:** Uncertainty caused by data shifts between the training and prediction set.

Bayesian methods capture epistemic uncertainty by modeling distributions over network weights. For instance, Bayesian Neural Networks (BNNs) (Jospin et al., 2022) sample from these distributions to produce multiple predictions, with the variability reflecting uncertainty. Deep Ensembles (Lakshminarayanan et al., 2017) and Monte Carlo Dropout (MCD) (Gal & Ghahramani, 2016) approximate this sampling via multiple models or stochastic weight activations within a single network. More recently, efficient Bayesian last-layer approaches such as Variational Bayesian Last Layers (Harrison et al., 2024) and Bayesian Non-negative Decision Layers (Hu et al., 2025) reduce computational cost by restricting stochasticity to the final layer. While Bayesian methods remain powerful, they typically require additional forward passes compared to deterministic models.

Evidential Deep Learning (EDL) methods (Ulmer et al., 2023; Amini et al., 2020) are more computationally efficient than Bayesian approaches, requiring only a single forward pass and one trained model. They assume the output follows a well-characterized distribution, predicting the parameters of the output distribution from which uncertainty can be derived. For classification, this corresponds to Dirichlet parameters (Sensoy et al., 2018), with Posterior Networks (PN) (Charpentier et al., 2020) extending this via normalizing flows. Despite capturing aleatoric and distributional uncertainty, these methods rely on restrictive assumptions about the output distribution.

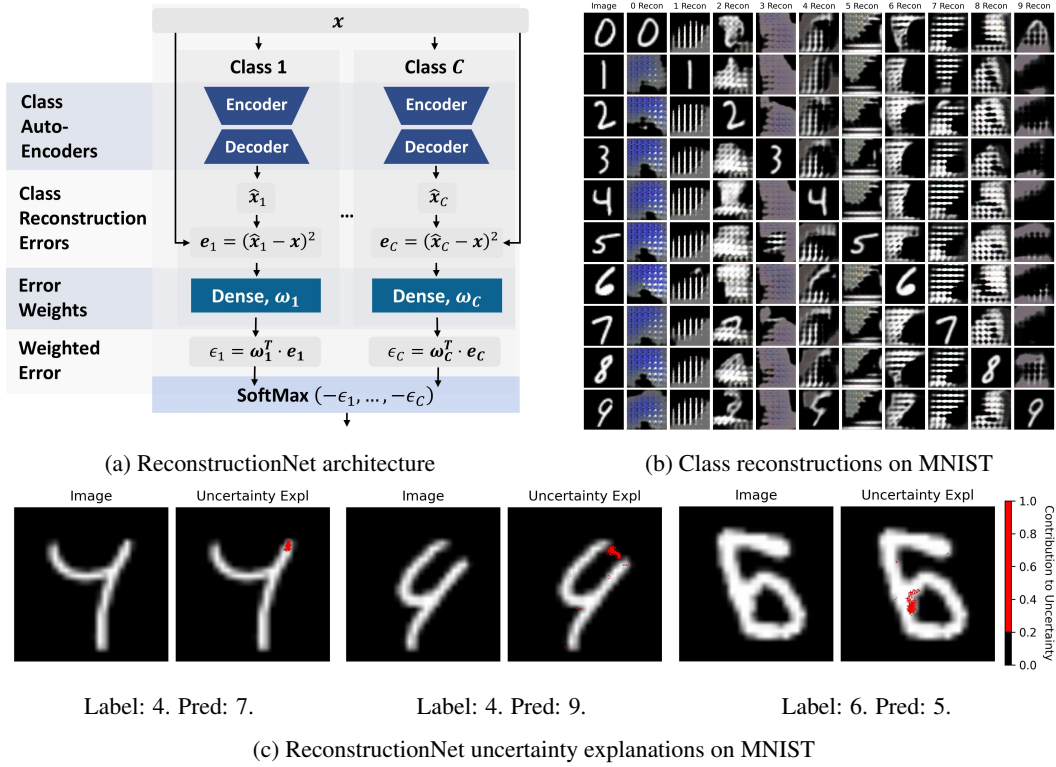
Deterministic Uncertainty Methods (DUMs) (Postels et al., 2022; Charpentier et al., 2023; Zelenka et al., 2023a) make minimal assumptions about the output distribution, estimating distributional uncertainty as the distance of an instance from the training set. A recent DUM, the Reconstruction Uncertainty Estimate (RUE) (Wang et al., 2024; Korte et al., 2024), uses a decoder to reconstruct inputs from the latent representation, with reconstruction error serving as the uncertainty measure. ReconstructionNet extends RUE by also capturing aleatoric uncertainty alongside distributional uncertainty.

108 2.2 UNCERTAINTY EXPLANATIONS
109110 Knowing when a model is unreliable is valuable, but uncertainty explanations provide deeper insight
111 by quantifying the contribution of each feature to the model’s overall uncertainty.
112113 **Definition 2 (Uncertainty Explanation)** *Given an instance $\mathbf{x} \in \mathbb{R}^d$, a model f , and an uncertainty
114 estimator $\sigma(\mathbf{x}; f) : \mathbb{R}^d \rightarrow \mathbb{R}$, an uncertainty explanation method $\zeta(\mathbf{x}; f, \sigma) : \mathbb{R}^d \rightarrow \mathbb{R}^d$ assigns each
115 input feature a real value reflecting its contribution to $f(\mathbf{x})$ ’s uncertainty.*
116117 Uncertainty explanation is a nascent field with two primary approaches:
118119 **Gradient-Based Methods** (Mougan & Nielsen, 2023; Iversen et al., 2024) applied standard eX-
120 plainable Artificial Intelligence (XAI) methods, such as Integrated Gradients (IG) (Sundararajan
121 et al., 2017), to explain uncertainty estimates. While easy to implement, gradient-based explana-
122 tions can be sparse due to vanishing gradients, making them difficult to interpret.
123124 **Perturbation-Based Methods** (Antorán et al., 2021; Wang et al., 2025) assess each feature’s contri-
125 bution to uncertainty by perturbing inputs and measuring the impact on the uncertainty score. Their
126 accuracy depends on the number of perturbations, making them computationally expensive.
127128 Both methods require an additional module for uncertainty explanation, increasing inference time.
129 In contrast, (Zelenka et al., 2023b) computes predictions, uncertainty, and explanations in a sin-
130 gle forward pass using one model. Based on prototype networks (Snell et al., 2017), it classifies
131 instances by similarity to class prototypes, with uncertainty explanations derived from the inner
132 product between the predicted prototype and the instance’s feature map. Similarly, Reconstruc-
133 tionNet leverages its architecture to provide ante-hoc uncertainty explanations efficiently during
134 inference.
135136 2.3 RECONSTRUCTION-BASED METHODS
137138 **Anomaly Detection.** Reconstruction error has been widely used in autoencoder-based anomaly
139 detection Chen et al. (2018) to identify deviations from the training distribution. While Reconstruc-
140 tionNet also leverages reconstruction errors, it differs substantially in several aspects:
141142 *Reconstruction for Classification and Uncertainty Estimation.* Traditional anomaly-detection au-
143 toencoders detect out-of-distribution (OOD) inputs only. In contrast, ReconstructionNet uses class-
144 specific autoencoders to model the joint input-output distribution and classifies by selecting the
145 class with the lowest reconstruction error. This reconstruction error also serves as a distributional
146 uncertainty estimate. Reconstruction thus supports both classification and uncertainty estimation in
147 ReconstructionNet.
148149 *Reconstruction Errors as Explanations.* Reconstruction errors in ReconstructionNet serve as
150 feature-level uncertainty explanations, highlighting which input features drive uncertainty, unlike
151 conventional anomaly detectors that produce only scalar anomaly scores.
152153 *Training Objective and Architecture.* Unlike unsupervised anomaly detection, Reconstruction-
154 Net uses a supervised training objective and class-specific autoencoders, where each class has its
155 own encoder-decoder pair. This design enables joint modeling of input-output distributions.
156157 **Reconstruction Error as Regularizers** Some works use reconstruction loss as a regularizer for
158 classification Le et al. (2018); Ghifary et al. (2016). ReconstructionNet differs fundamentally in
159 several aspects:
160161 *Class-specific autoencoders and joint distribution modeling.* Prior works use a single autoencoder
162 with conditional probabilities for classification. ReconstructionNet employs one autoencoder per
163 class to model the joint input-output distribution, classifying via minimum reconstruction error.
164165 *Uncertainty estimation and explanations.* Unlike prior works, ReconstructionNet leverages recon-
166 struction errors to quantify uncertainty and provide feature-level explanations.
167168 *Distinct architecture and prediction mechanism.* Instead of connecting encoders directly to the
169 prediction head, ReconstructionNet computes weighted reconstruction errors across class-specific
170 autoencoders to make predictions.
171

162 3 METHODOLOGY 163

164 We present ReconstructionNet, a neural network architecture which offers the following features:
165

- 166 1. Uses the joint input-output probability for classification.
- 167 2. Quantifies distributional and aleatoric uncertainty.
- 168 3. Generates uncertainty explanations.



195 Figure 1: ReconstructionNet overview and examples. (a) ReconstructionNet architecture: Each
196 class-specific autoencoder is trained to reconstruct only its own class, producing reconstruction
197 errors inversely related to the joint input–output probability. After applying error weights and softmax
198 normalization, the resulting probabilities are used for classification (Equation 2). (b) MNIST class
199 reconstructions: Only the autoencoder for the true class yields a faithful reconstruction, leading to
200 lower reconstruction error and a higher prediction probability. Other autoencoders generate artifacts
201 (e.g., checkerboard patterns (Odena et al., 2016)) due to lack of training on mismatched classes. (c)
202 MNIST uncertainty explanations: Weighted class reconstruction errors highlight uncertain regions.
203 In the first example, the extra right vertical line increases uncertainty of it being a 7; in the middle,
204 the missing connector raises uncertainty of it being a 9; in the last, the extra bottom-left vertical line
205 increases uncertainty of it being a 5. See Appendix A.4 for implementation details.

207 3.1 CLASSIFICATION 208

209 Consider a classification dataset with N instances and C classes, where each instance i has an input
210 vector $\mathbf{x}_i \in \mathbb{R}^d$ and label y_i . Let \mathcal{X}_j denote the set of training instances with target label j , containing
211 N_j instances. For each instance i and class j , the true and predicted class probabilities are p_{ij} and
212 \hat{p}_{ij} , respectively.

213 Traditional neural networks predict the conditional probability of class j given instance \mathbf{x}_i . The
214 class with the highest conditional probability is then selected as the final predicted class \hat{y}_i :

$$215 \hat{y}_i = \arg \max_{j \in \{1, \dots, C\}} \Pr(\hat{y}_i = j | \mathbf{x}_i). \quad (1)$$

ReconstructionNet differs from traditional feedforward neural network classifiers in its inference process. ReconstructionNet instead predicts the joint probability of the target \hat{y}_i and input \mathbf{x}_i and the target class with the highest joint probability is the final predicted class (Equation 2):

$$\hat{y}_i = \arg \max_{j \in \{1, \dots, C\}} \Pr(\hat{y}_i = j, \mathbf{x}_i). \quad (2)$$

Equation 2 is a valid classification formulation, equivalent to Equation 1 via Bayes' theorem:

$$\arg \max_j \Pr(\hat{y}_i = j, \mathbf{x}_i) = \arg \max_j \Pr(\hat{y}_i = j | \mathbf{x}_i) \Pr(\mathbf{x}_i) = \arg \max_j \Pr(\hat{y}_i = j | \mathbf{x}_i). \quad (3)$$

To model joint input-output probability, we adopt the model architecture in Figure 1a. Given a classification problem with C classes, we construct C autoencoders g_1, \dots, g_C and train them simultaneously, such that each autoencoder models the joint probability $\Pr(\hat{y}_i = j, \mathbf{x}_i)$. During inference, the model computes feature-wise reconstruction errors \mathbf{e}_{ij} for each autoencoder (Equation 4). $\hat{\mathbf{x}}_{ij} = g_j(\mathbf{x}_i)$ is the reconstructed input of instance i by class- j autoencoder g_j ; $\hat{\mathbf{x}}_{ij}^k$ is the reconstruction for feature k .

$$\mathbf{e}_{ij} = \begin{bmatrix} (\hat{\mathbf{x}}_{ij}^1 - \mathbf{x}_i^1)^2 & \dots & (\hat{\mathbf{x}}_{ij}^d - \mathbf{x}_i^d)^2 \end{bmatrix} \quad (4)$$

Next, it calculates a weighted reconstruction error ϵ_{ij} for each class j , where the weights ω_j are trainable parameters (Equation 5).

$$\epsilon_{ij} = \omega_j^\top \cdot \mathbf{e}_{ij}. \quad (5)$$

Finally, prediction probability \hat{p}_{ij} is obtained by applying softmax to the negative weighted errors ϵ_i . Negation is used since the higher the reconstruction error, the lower the probability (Figure 1b).

$$\hat{p}_i = \text{softmax}(-\epsilon_i). \quad (6)$$

To train the ensemble of class autoencoders concurrently, we designed a loss function (Equation 7) consisting of two components, with β as a hyperparameter to balance both training objectives.

$$\mathcal{L}_{total} = \mathcal{L}_{CE} + \beta \cdot \mathcal{L}_{Class_MSE}, \quad \mathcal{L}_{CE} = - \sum_{i=1}^N \sum_{j=1}^C p_{ij} \log(\hat{p}_{ij}) \quad (7)$$

\mathcal{L}_{CE} is the cross-entropy loss; it optimizes the classification performance of the ReconstructionNet. To ensure that the class autoencoders also learn to model the joint probability $\Pr(\hat{y}_i = j, \mathbf{x}_i)$ while also maintaining predictive accuracy, we introduce the class-dependent mean squared error (MSE):

$$\mathcal{L}_{Class_MSE}^j = \frac{1}{N_j} \sum_{\mathbf{x}_i \in \mathcal{X}_j} \|\hat{\mathbf{x}}_{ij} - \mathbf{x}_i\|^2. \quad (8)$$

Where each class autoencoder g_j is trained to minimize reconstruction error for its corresponding instances in \mathcal{X}_j . The overall reconstruction loss, \mathcal{L}_{Class_MSE} , is then the average across all classes:

$$\mathcal{L}_{Class_MSE} = \frac{1}{N} \sum_{j=1}^C N_j \cdot \mathcal{L}_{Class_MSE}^j. \quad (9)$$

The formulation of \mathcal{L}_{Class_MSE} ensures each class autoencoder is trained exclusively to reconstruct samples from its ground truth class, thereby modeling the joint distribution of the input and target. Assume that the latent vector z_j from the encoder of class j follows an isotropic Gaussian distribution, $\Pr(\mathbf{x}_i, y_i = j | z_{ij}) = \mathcal{N}(\hat{\mathbf{x}}, \sigma^2 I)$ (Doersch, 2021; Odaibo, 2019). The probability density function of the distribution of all \mathbf{x} from class j can be expressed as:

$$\Pr(\mathbf{x}_i, y_i = j | z_{ij}) = \frac{1}{(2\pi\sigma^2)^{d/2}} \exp\left(-\frac{1}{2\sigma^2} \|\mathbf{x}_i - \hat{\mathbf{x}}_{ij}\|^2\right). \quad (10)$$

To model this distribution, we optimize our model to maximize the log-likelihood over the training dataset with target class j :

$$\ell(\hat{\mathbf{x}}, \sigma) = \sum_{i \in \mathcal{X}_j} \left[-\frac{d}{2} \log(2\pi\sigma^2) - \frac{1}{2\sigma^2} \|\mathbf{x}_i - \hat{\mathbf{x}}_{ij}\|^2 \right] \quad (11)$$

$$= \sum_{i \in \mathcal{X}_j} \left[-\frac{d}{2} \log(2\pi\sigma^2) \right] - \frac{N_j}{2\sigma^2} \cdot \mathcal{L}_{Class_MSE}^j. \quad (12)$$

We observe that maximizing the log-likelihood is equivalent to minimizing $\mathcal{L}_{Class_MSE}^j$. This demonstrates that minimizing \mathcal{L}_{Class_MSE} leads to the training of class autoencoders that model the joint distribution of the input and target, with reconstruction error inversely related to the joint probability. Additionally, the architecture and loss function of ReconstructionNet limit its hypothesis space, making it more resistant to epistemic uncertainty (Hüllermeier & Waegeman, 2021).

3.2 UNCERTAINTY ESTIMATION

By modelling the joint input-output probability, we can quantify:

1. **Aleatoric Uncertainty:** When instances lie in overlapping class regions, several classes have similarly *high* probabilities above threshold θ_1 , signalling high aleatoric uncertainty.

$$\exists \mathbf{C}_i \subseteq \{1, \dots, C\}, |\mathbf{C}_i| \geq 2 \text{ s.t.}$$

$$\Pr(\hat{y}_i = c_1, \mathbf{x}_i) \approx \Pr(\hat{y}_i = c_2, \mathbf{x}_i) \geq \theta_1, \forall c_1, c_2 \in \mathbf{C}_i. \quad (13)$$

2. **Distributional Uncertainty:** When instances lie beyond the training distribution, the joint probabilities of all classes are similarly *low*, below some threshold θ_2 , signaling high distributional uncertainty.

$$\forall c \in \{1, \dots, C\}, \Pr(\hat{y}_i = c, \mathbf{x}_i) \leq \theta_2. \quad (14)$$

Modelling joint probabilities allows differentiation between uncertainty types: instances show high aleatoric uncertainty when their most probable classes have probabilities above θ_1 , and high distributional uncertainty when all class probabilities are below θ_2 .

The notion of aleatoric uncertainty, as illustrated in Equation 13, is nicely captured by Shannon entropy, reflecting evenly spread high prediction probabilities across overlapping classes:

Definition 3 (Aleatoric Uncertainty) *For an instance \mathbf{x}_i , aleatoric uncertainty is quantified using the Shannon entropy (Shannon, 1948) of the prediction probabilities \hat{p}_{ij} :*

$$\sigma_{aleatoric}(\mathbf{x}_i) = - \sum_{j=1}^C \hat{p}_{ij} \log \hat{p}_{ij}.$$

Distributional uncertainty in Equation 14 is captured by the predicted class's reconstruction error. By design, the predicted class has the lowest error and highest probability among all classes; therefore, if its error is high (probability low), all other classes also have low probabilities.

Definition 4 (Distributional Uncertainty) *For an instance \mathbf{x}_i , distributional uncertainty is the reconstruction error of the predicted class \hat{y}_i 's autoencoder:*

$$\sigma_{dist}(\mathbf{x}_i) = \|\mathbf{e}_{i\hat{y}_i}\|_1.$$

3.3 UNCERTAINTY EXPLANATION

The weighted reconstruction errors ζ of the predicted class \hat{y} serve as uncertainty explanations, as they represent feature uncertainties scaled by their importance to the prediction.

Definition 5 (ReconstructionNet Explanation) *The ReconstructionNet Explanation for instance \mathbf{x}_i and its predicted class \hat{y}_i is the weighted reconstruction errors of predicted class \hat{y}_i :*

$$\zeta(\mathbf{x}_i) = \omega_{\hat{y}_i} \odot \mathbf{e}_{i\hat{y}_i}.$$

ReconstructionNet uncertainty explanations exhibit the following three properties: (1) Implementation Invariance (Sundararajan et al., 2017), (2) Sensitivity (Sundararajan et al., 2017), and (3) Consistency (Lundberg & Lee, 2017). An explanation that satisfies all three properties is (1) consistent across different implementations, (2) does not attribute irrelevant features incorrectly, and (3) preserves the relative importance of features across models.

An uncertainty explanation is *implementation-invariant* if, for a pair of functionally equivalent prediction models, the same explanation is generated for any instance. A pair of functionally equivalent models are models that yield the same output for a given set of inputs.

324 **Property 1 (Implementation Invariance)** *Given two functionally equivalent prediction models, f
 325 and f' , an explanation function χ is implementation-invariant if and only if, for any instance \mathbf{x} , the
 326 explanations derived from both models using χ are equivalent: $\chi(\mathbf{x}; f) = \chi(\mathbf{x}; f')$.*

328 ReconstructionNet’s uncertainty explanations ζ , defined as the weighted reconstruction errors of the
 329 predicted class (Definition 5), are implementation-invariant: for two functionally equivalent models,
 330 both the error weights ω and the reconstruction errors remain identical.

331 A *sensitive* explanation function allocates zero attribution to irrelevant features for prediction. A
 332 feature is considered irrelevant if a change in its value does not impact the model’s prediction.
 333

334 **Property 2 (Sensitivity)** *An explanation function χ is sensitive if it assigns a zero feature attribu-
 335 tion value, $\chi(\mathbf{x}; f)_i = 0$, to features i that are irrelevant to the prediction.*

337 ReconstructionNet’s uncertainty explanations ζ are sensitive. Since the error weight ω encodes each
 338 feature’s contribution to the final prediction, any change in feature uncertainty that does not affect
 339 the prediction must have a weight of zero, yielding a weighted reconstruction error ζ of zero.

340 An explanation is *consistent* if a feature’s uncertainty attribution does not decrease when the model
 341 is altered to increase that feature’s contribution.

343 **Property 3 (Consistency)** *Let f' be a modification of f where feature i ’s contribution is increased.
 344 For an instance \mathbf{x} and $\mathbf{x}^{\setminus i}$ with $x_i = 0$, an explanation χ is consistent if:*

$$345 \quad f'(\mathbf{x}) - f'(\mathbf{x}^{\setminus i}) \geq f(\mathbf{x}) - f(\mathbf{x}^{\setminus i}) \quad \text{then} \quad \chi(\mathbf{x}; f')_i \geq \chi(\mathbf{x}; f)_i.$$

348 ReconstructionNet’s uncertainty explanations, ζ , are consistent. For any instance, reconstruction
 349 errors stay the same between f and f' , since the joint input-output probability modeled by the
 350 autoencoders is independent of feature contributions. Thus, only the error weights ω can change; if
 351 a feature’s weight increases in f' , its uncertainty attribution also increases, satisfying consistency.

353 4 EXPERIMENTS

355 4.1 DATASETS

357 We use tabular datasets (Covid, Diabetes, Fund) to evaluate uncertainty reliability, selectivity, and ro-
 358 bustness, medical image datasets (ISIC, OCTMNIST) for OOD detection, and MNIST, ISIC, Covid
 359 and Diabetes to assess uncertainty explanation correctness. The datasets are summarized as follows:
 360

- 361 1. **Covid** (Hinns et al., 2021) is a tabular dataset of United Kingdom’s COVID-19 policies
 362 and regional case counts, labelled by whether R_t (effective reproduction number) > 1 .
- 363 2. **Diabetes** (Mustafa, 2023) is a binary tabular dataset of demographics, pre-existing condi-
 364 tions, and vital signs, with labels indicating diabetes status.
- 366 3. **Fund** (Kovvuri et al., 2023) is a binary tabular dataset from 4,330 funds, using macroe-
 367 conomic indicators, fund allocations, HHI, and past performance to predict if a fund’s net
 368 asset value (NAV) exceeds the previous quarter’s.
- 369 4. **ISIC** (Codella et al., 2019; Tschandl et al., 2018) is a dermoscopic image dataset of seven
 370 skin conditions. For OOD detection, we created three datasets with decreasing similarity
 371 to ISIC: BCN-IN (images from seen classes of BCN20000 (Combalia et al., 2019)), BCN-
 372 OUT (images from the unseen Scar class), and ChestMNIST (Wang et al., 2017).
- 373 5. **OCTMNIST** (Kermany et al., 2018) is a retinal OCT dataset with four classes. For OOD
 374 detection, we used three datasets of decreasing similarity to OCTMNIST: OCTDL-IN (im-
 375 ages from seen classes of OCTDL (Kulyabin et al., 2024)), OCTDL-OUT (images from
 376 unseen classes), and ChestMNIST (Wang et al., 2017).
- 377 6. **MNIST** (Deng, 2012) is an image dataset of ten handwritten digits.

378 4.2 BASELINES
379

380 We compared ReconstructionNet against six recent state-of-the-art uncertainty estimation methods:
 381 (1) Entropy, (2) MCD, (3) DE, (4) PN, (5) BNN, and (6) EDL. Implementation and tuning details of
 382 the baselines are provided in the appendix.

383 4.3 EVALUATION METRICS
384

385 We evaluate prediction performance with Area Under receiver operating characteristic Curve (AUC)
 386 and accuracy. To evaluate uncertainty estimation performance, we used the following metrics:
 387

- 388 1. **Correlation** (Mi et al., 2022; Upadhyay et al., 2022) measures reliability as the Pearson
 389 correlation between uncertainty and error, with higher values indicating better reliability.
- 390 2. **AURC** (Ding et al., 2020) quantifies selectivity by measuring the area under the risk-
 391 coverage curve (AURC), with lower values indicating better selectivity.
- 392 3. σ -**Risk Score** measures robustness to false negatives as errors for instances with normalized
 393 uncertainty below $\sigma = \{0.1, 0.2, 0.3, 0.4\}$, with lower values indicating greater resilience.
- 394 4. **OOD Detection** (Lakshminarayanan et al., 2017; Postels et al., 2020; Malinin & Gales,
 395 2018) measures how well uncertainty distinguishes in-distribution from OOD instances
 396 using AUROC, with higher values indicating better detection.

397 4.4 RESULTS
398400 4.4.1 PREDICTION PERFORMANCE
401

402 Table 1: Model prediction performance. NN refers to an MLP for tabular and a ResNet for image
 403 datasets. The best-performing model for each metric is **bolded**, while the second-best is underlined.
 404

	Covid (Tabular)		Diabetes (Tabular)		Fund (Tabular)		ISIC (Image)		OCTMNIST (Image)	
	AUC (↑)	Acc (↑)								
RN (Ours)	<u>0.95 ± 0.00</u>	<u>0.88 ± 0.00</u>	<u>0.97 ± 0.00</u>	<u>0.92 ± 0.01</u>	0.75 ± 0.01	0.71 ± 0.00	0.91 ± 0.01	0.76 ± 0.01	0.99 ± 0.00	0.91 ± 0.02
NN	0.95 ± 0.00	0.89 ± 0.00	0.98 ± 0.00	0.93 ± 0.01	0.60 ± 0.02	0.71 ± 0.00	0.87 ± 0.01	0.70 ± 0.01	0.99 ± 0.01	0.88 ± 0.03
MCD	0.95 ± 0.00	0.89 ± 0.00	0.98 ± 0.00	0.93 ± 0.01	0.59 ± 0.02	0.71 ± 0.00	0.87 ± 0.01	0.70 ± 0.01	0.99 ± 0.01	0.88 ± 0.03
DE	0.95 ± 0.00	0.89 ± 0.00	0.98 ± 0.00	0.93 ± 0.00	0.59 ± 0.01	0.71 ± 0.00	0.89 ± 0.00	0.72 ± 0.01	0.99 ± 0.00	0.89 ± 0.02
PN	0.96 ± 0.01	0.88 ± 0.01	0.97 ± 0.00	0.92 ± 0.01	0.53 ± 0.00	0.71 ± 0.00	0.70 ± 0.01	0.64 ± 0.01	0.94 ± 0.02	0.80 ± 0.05
BNN	0.91 ± 0.02	0.85 ± 0.02	0.97 ± 0.01	0.91 ± 0.01	0.54 ± 0.01	0.71 ± 0.00	0.60 ± 0.02	0.52 ± 0.02	0.99 ± 0.00	0.87 ± 0.02
EDL	0.92 ± 0.02	0.79 ± 0.18	0.87 ± 0.07	0.95 ± 0.02	0.58 ± 0.05	<u>0.62 ± 0.17</u>	0.53 ± 0.01	0.51 ± 0.01	<u>0.96 ± 0.00</u>	0.83 ± 0.02

414 Table 1 compares model performance. ReconstructionNet (RN) achieved strong results across
 415 datasets, with second-highest AUC and accuracy on COVID and Diabetes, and the highest AUC
 416 and accuracy on Fund, ISIC, and OCTMNIST. Notably, on Fund, ReconstructionNet outperformed
 417 others in AUC despite similar accuracy, suggesting it learns discriminative features robust to data
 418 shifts (caused by the COVID-19 pandemic) and is resilient to epistemic uncertainty.

419 4.4.2 UNCERTAINTY ESTIMATION PERFORMANCE
420

421 **Aleatoric Uncertainty:** Table 2 summarizes uncertainty estimation performance. Reconstruction-
 422 Net outperformed all models on COVID except σ -risk at $\sigma = 0.1$, where it matched MLP Entropy
 423 and MCD. On Diabetes and Fund, it consistently ranked among the top across metrics.
 424

425 **Distributional Uncertainty:** Table 3 presents the OOD detection performance of all uncertainty
 426 estimates. ReconstructionNet achieves the highest AUROC across all OOD datasets and improves
 427 as datasets deviate further from in-distribution data, showing it effectively ranks dataset dissimilarity.
 428 In contrast, other estimates like Entropy, MCD, PN, and BNN drop on highly dissimilar datasets (see
 429 ISIC) or struggle with unseen classes, as seen on OCTMNIST.

430 **Distinguishing Between Aleatoric and Distributional:** To illustrate ReconstructionNet’s ability
 431 to separate uncertainty types, we visualize aleatoric and distributional uncertainty over time on the
 432 Fund dataset (Figure 2). Aleatoric uncertainty is highest before January 2020, while during the 2020

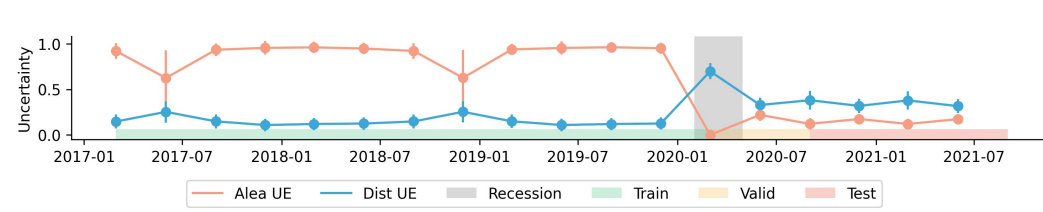
432 Table 2: Uncertainty estimation performance. The best-performing model for each metric is **bolded**,
 433 while the second-best model is underlined.

Data	UE	Correlation (\uparrow)	AURC (\downarrow)	$\sigma = 0.1$ (\downarrow)	$\sigma = 0.2$ (\downarrow)	$\sigma = 0.3$ (\downarrow)	$\sigma = 0.4$ (\downarrow)
Covid	RN (Ours)	0.823 ± 0.016	0.028 ± 0.002	0.005 ± 0.001	0.006 ± 0.002	0.007 ± 0.002	0.012 ± 0.005
	MLP Entropy	0.664 ± 0.012	0.030 ± 0.002	0.003 ± 0.004	0.016 ± 0.006	0.022 ± 0.006	0.032 ± 0.005
	MLP MCD	0.639 ± 0.012	0.032 ± 0.003	0.004 ± 0.005	0.018 ± 0.009	0.029 ± 0.006	0.042 ± 0.005
	MLP DE	0.603 ± 0.031	0.030 ± 0.003	0.011 ± 0.003	0.020 ± 0.007	0.032 ± 0.007	0.040 ± 0.005
	PN Epis	0.313 ± 0.082	0.038 ± 0.011	0.021 ± 0.010	0.034 ± 0.015	0.041 ± 0.017	0.051 ± 0.016
	PN Alea	0.690 ± 0.034	0.029 ± 0.007	0.016 ± 0.005	0.022 ± 0.007	0.032 ± 0.006	0.039 ± 0.005
	BNN	0.030 ± 0.027	0.132 ± 0.018	0.104 ± 0.070	0.159 ± 0.023	0.161 ± 0.023	0.132 ± 0.015
Diabetes	EDL	0.674 ± 0.068	0.115 ± 0.094	0.238 ± 0.105	0.073 ± 0.009	0.058 ± 0.004	0.045 ± 0.005
	RN (Ours)	0.902 ± 0.011	0.008 ± 0.001	0.000 ± 0.000	0.001 ± 0.000	0.001 ± 0.000	0.001 ± 0.000
	MLP Entropy	0.864 ± 0.009	0.007 ± 0.002	0.000 ± 0.000	0.000 ± 0.000	0.001 ± 0.000	0.001 ± 0.000
	MLP MCD	0.845 ± 0.022	0.008 ± 0.002	0.000 ± 0.000	0.000 ± 0.000	0.001 ± 0.000	0.002 ± 0.001
	MLP DE	0.733 ± 0.031	0.011 ± 0.001	0.000 ± 0.000	0.001 ± 0.000	0.005 ± 0.001	0.011 ± 0.003
	PN Epis	0.525 ± 0.297	0.020 ± 0.021	0.006 ± 0.009	0.016 ± 0.023	0.023 ± 0.030	0.028 ± 0.033
	PN Alea	0.812 ± 0.022	0.009 ± 0.001	0.001 ± 0.000	0.001 ± 0.000	0.002 ± 0.001	0.003 ± 0.001
Fund	BNN	-0.619 ± 0.012	0.214 ± 0.016	0.262 ± 0.024	0.222 ± 0.016	0.185 ± 0.016	0.136 ± 0.013
	EDL	0.942 ± 0.017	0.046 ± 0.034	0.000 ± 0.000	0.001 ± 0.002	0.006 ± 0.006	0.011 ± 0.010
	RN (Ours)	0.385 ± 0.008	0.141 ± 0.003	0.039 ± 0.004	0.048 ± 0.005	0.077 ± 0.015	0.126 ± 0.023
	MLP Entropy	0.131 ± 0.034	0.212 ± 0.023	0.064 ± 0.043	0.132 ± 0.063	0.187 ± 0.036	0.241 ± 0.012
	MLP MCD	0.128 ± 0.038	0.236 ± 0.018	0.073 ± 0.067	0.124 ± 0.062	0.165 ± 0.046	0.210 ± 0.028
	MLP DE	0.022 ± 0.045	0.287 ± 0.032	0.364 ± 0.331	0.330 ± 0.192	0.283 ± 0.031	0.286 ± 0.045
	PN Epis	0.016 ± 0.001	0.291 ± 0.017	0.279 ± 0.028	0.278 ± 0.025	0.278 ± 0.022	0.279 ± 0.021
Fund	PN Alea	0.166 ± 0.026	0.271 ± 0.001	0.221 ± 0.007	0.225 ± 0.009	0.230 ± 0.013	0.235 ± 0.009
	BNN	-0.198 ± 0.028	0.364 ± 0.010	0.665 ± 0.189	0.543 ± 0.125	0.442 ± 0.065	0.405 ± 0.026
	EDL	0.162 ± 0.118	0.301 ± 0.202	0.016 ± 0.015	0.055 ± 0.062	0.101 ± 0.078	0.174 ± 0.092

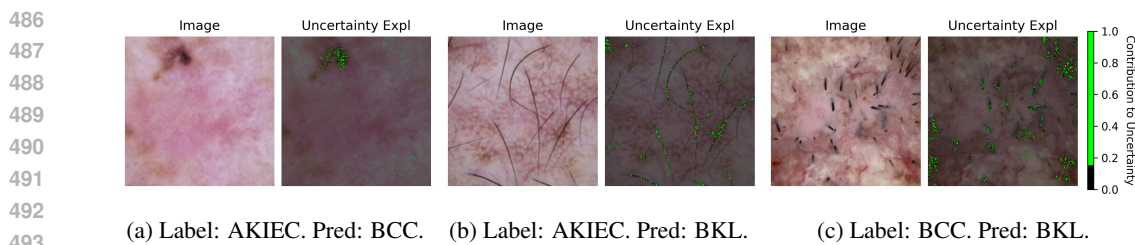
455
 456 Table 3: Out-of-distribution (OOD) detection performance, measured using AUROC. OOD datasets
 457 are presented in order of increasing deviation from the in-distribution. The best-performing model
 458 for each metric is **bolded**, while the second-best model is underlined.
 459

	ISIC			OCTMNIST		
	BCN-IN (\uparrow)	BCN-OUT (\uparrow)	ChestMNIST (\uparrow)	OCTDL-IN (\uparrow)	OCTDL-OUT (\uparrow)	ChestMNIST (\uparrow)
RN (Ours)	0.777 ± 0.086	0.846 ± 0.070	0.919 ± 0.097	0.783 ± 0.082	0.866 ± 0.049	1.000 ± 0.000
ResNet Entropy	0.742 ± 0.010	0.757 ± 0.027	0.664 ± 0.072	0.674 ± 0.031	0.386 ± 0.066	0.826 ± 0.060
ResNet MCD	0.746 ± 0.004	0.770 ± 0.016	0.678 ± 0.080	0.661 ± 0.034	0.392 ± 0.064	0.844 ± 0.060
ResNet DE	0.720 ± 0.020	0.703 ± 0.029	0.728 ± 0.055	0.739 ± 0.009	0.497 ± 0.029	0.900 ± 0.028
PN Epis	0.674 ± 0.021	0.686 ± 0.039	0.654 ± 0.050	0.565 ± 0.052	0.483 ± 0.087	0.470 ± 0.145
PN Alea	0.660 ± 0.026	0.669 ± 0.041	0.631 ± 0.065	0.625 ± 0.063	0.492 ± 0.025	0.500 ± 0.107
BNN	0.556 ± 0.011	0.540 ± 0.056	0.547 ± 0.059	0.742 ± 0.014	0.734 ± 0.016	0.896 ± 0.015
EDL	0.533 ± 0.011	0.539 ± 0.023	0.619 ± 0.024	0.633 ± 0.012	0.669 ± 0.011	0.760 ± 0.013

471 recession (per the National Bureau of Economic Research), distributional uncertainty predominates,
 472 demonstrating ReconstructionNet’s discriminative capability.
 473



482 Figure 2: Aleatoric (Alea) and distributional (Dist) uncertainty over time on the Fund dataset. Un-
 483 certainty values are min–max normalized, and error bars represent one standard deviation. In early
 484 2020, distributional uncertainty overtook aleatoric uncertainty due to COVID-19-induced shifts,
 485 while aleatoric uncertainty dropped as increasing class imbalance reduced label ambiguity.



(a) Label: AKIEC. Pred: BCC. (b) Label: AKIEC. Pred: BKL. (c) Label: BCC. Pred: BKL.

Figure 3: Uncertainty explanation illustration using images from the ISIC dataset. Positive attributions were min–max normalized, thresholded (pixel uncertainty > 0.15 shown in green), and overlaid for clarity. The highlighted regions “explain” the prediction uncertainty. AKIEC refers to Actinic Keratosis, BCC to Basal Cell Carcinoma, and BKL to Benign Keratosis.

4.4.3 UNCERTAINTY EXPLANATION PERFORMANCE

To highlight the practical value of our uncertainty explanations in identifying regions that contribute to misclassification, we qualitatively assess them on the ISIC dataset. In Figure 3a, the image was misclassified as BCC instead of AKIEC, with uncertainty concentrated on the mole at the top-left corner, likely because such dark, mole-like spots resemble features more typical of BCC than AKIEC (Lee, 2017). In Figures 3b and 3c, both images were misclassified as BKL, with uncertainty concentrated on the hairs covering a substantial portion of the lesion, as such occlusions can obscure diagnostic features. These visual explanations align with human intuition, demonstrating their effectiveness in pinpointing input features that confuse the model.

Table 4: Top-k accuracy of each uncertainty-explanation method in identifying perturbed features on the Covid and Diabetes datasets.

Method	Covid			Diabetes		
	Top-1 Acc	Top-3 Acc	Top-5 Acc	Top-1 Acc	Top-3 Acc	Top-5 Acc
IG	0.163 ± 0.003	0.355 ± 0.017	0.436 ± 0.020	0.065 ± 0.008	0.221 ± 0.005	0.446 ± 0.022
SHAP	0.102 ± 0.011	0.193 ± 0.020	0.262 ± 0.017	0.093 ± 0.004	0.247 ± 0.008	0.387 ± 0.014
RN (Ours)	0.437 ± 0.035	0.604 ± 0.027	0.646 ± 0.023	0.272 ± 0.064	0.509 ± 0.045	0.599 ± 0.040

We also evaluate the performance of our uncertainty explanations on tabular data using the covariate-shift experiment from Watson et al. (2023). For each test instance, we randomly perturb one feature by adding noise drawn from $\mathcal{N}(0.5, 0.1)$ and assess whether an explanation ranks this perturbed feature among its top-k most uncertain features (Top-k Accuracy). This directly measures whether the explanation identifies the feature contributing to distributional uncertainty.

We compare ReconstructionNet (RN) explanations with: (1) Integrated Gradients (IG), a gradient-based method, and (2) KernelSHAP, a perturbation-based method, both applied to explain the entropy of ReconstructionNet’s predictive distribution (Iversen et al., 2024). Across the COVID and Diabetes datasets (Table 4), RN achieves consistently higher top-k accuracy for all k , demonstrating its effectiveness in localizing the source of uncertainty.

5 CONCLUSION

This paper proposed ReconstructionNet, a neural network for reliable uncertainty estimation alongside classification. Unlike models based on conditional probability, ReconstructionNet uses class-specific autoencoders to model the input–output joint distribution, predicting the class with maximal joint probability (or minimal reconstruction error). This approach quantifies aleatoric and distributional uncertainty while minimizing epistemic uncertainty in a single training session. Across five real-world datasets, ReconstructionNet achieved comparable or improved classification performance, with uncertainty estimates showing superior reliability, selectivity, robustness to false negatives, and strong OOD detection. Its inbuilt, cost-free explanations highlight input features contributing to uncertainty, with theoretical properties of (1) Implementation Invariance, (2) Sensitivity, and (3) Consistency. While ReconstructionNet performs best on large, balanced datasets, this limitation suggests future directions, such as quantifying epistemic uncertainty.

540 **6 REPRODUCIBILITY STATEMENT**
 541

542 For implementation details, see the code repository: [https://anonymous.4open.
 543 science/r/ReconstructionNet-4F8C/](https://anonymous.4open.science/r/ReconstructionNet-4F8C/). For tabular datasets, input features were normal-
 544 ized using min–max scaling prior to training. For image datasets, pixel intensities were scaled from
 545 [0, 255] to [0, 1].
 546

547 **REFERENCES**
 548

- 549 Alexander Amini, Wilko Schwarting, Ava Soleimany, and Daniela Rus. Deep eviden-
 550 tial regression. In Hugo Larochelle, Marc’Aurelio Ranzato, Raia Hadsell, Maria-Florina
 551 Balcan, and Hsuan-Tien Lin (eds.), *Advances in Neural Information Processing Sys-
 552 tems 33: Annual Conference on Neural Information Processing Systems 2020, NeurIPS
 553 2020, December 6-12, 2020, virtual, volume 33, pp. 14927–14937, virtual, 2020. Curran
 554 Associates, Inc. URL [https://proceedings.neurips.cc/paper/2020/hash/
 555 aab085461de182608ee9f607f3f7d18f-Abstract.html](https://proceedings.neurips.cc/paper/2020/hash/aab085461de182608ee9f607f3f7d18f-Abstract.html).*
- 556 Javier Antorán, Umang Bhatt, Tameem Adel, Adrian Weller, and José Miguel Hernández-Lobato.
 557 Getting a CLUE: A method for explaining uncertainty estimates. In *9th International Conference
 558 on Learning Representations, ICLR 2021, Virtual Event, Austria, May 3-7, 2021, Austria, 2021.*
 559 OpenReview.net. URL <https://openreview.net/forum?id=XSLF1XFq5h>.
- 560 Jane Bromley, Isabelle Guyon, Yann LeCun, Eduard Säckinger, and Roopak Shah.
 561 Signature Verification using a ”Siamese” Time Delay Neural Network. In *Ad-
 562 vances in Neural Information Processing Systems*, volume 6, USA, 1993. Morgan-
 563 Kaufmann. URL [https://proceedings.neurips.cc/paper_files/paper/
 564 1993/hash/288cc0ff022877bd3df94bc9360b9c5d-Abstract.html](https://proceedings.neurips.cc/paper_files/paper/1993/hash/288cc0ff022877bd3df94bc9360b9c5d-Abstract.html).
- 565 Bertrand Charpentier, Daniel Zügner, and Stephan Günnemann. Posterior Network: Uncertainty
 566 Estimation without OOD Samples via Density-Based Pseudo-Counts. In *Advances in Neural
 567 Information Processing Systems*, volume 33, pp. 1356–1367, Online, 2020. Curran Associates,
 568 Inc.
- 569 Bertrand Charpentier, Chenxiang Zhang, and Stephan Günnemann. Training, architecture, and prior
 570 for deterministic uncertainty methods. *CoRR*, abs/2303.05796, 2023. doi: 10.48550/ARXIV.
 571 2303.05796. URL <https://doi.org/10.48550/arXiv.2303.05796>.
- 573 Nitesh V Chawla, Kevin W Bowyer, Lawrence O Hall, and W Philip Kegelmeyer. Smote: synthetic
 574 minority over-sampling technique. *Journal of artificial intelligence research*, 16:321–357, 2002.
- 575 Zhaomin Chen, Chai Kiat Yeo, Bu Sung Lee, and Chiew Tong Lau. Autoencoder-based network
 576 anomaly detection. In *2018 Wireless telecommunications symposium (WTS)*, pp. 1–5. IEEE, 2018.
- 578 Sumit Chopra, Raia Hadsell, and Yann LeCun. Learning a similarity metric discriminatively, with
 579 application to face verification. In *2005 IEEE computer society conference on computer vision
 580 and pattern recognition (CVPR’05)*, volume 1, pp. 539–546, USA, 2005. IEEE.
- 581 Noel Codella, Veronica Rotemberg, Philipp Tschandl, M. Emre Celebi, Stephen Dusza, David Gut-
 582 man, Brian Helba, Aadi Kalloo, Konstantinos Liopyris, Michael Marchetti, Harald Kittler, and
 583 Allan Halpern. Skin Lesion Analysis Toward Melanoma Detection 2018: A Challenge Hosted by
 584 the International Skin Imaging Collaboration (ISIC), March 2019.
- 585 Marc Combalià, Noel CF Codella, Veronica Rotemberg, Brian Helba, Veronica Vilaplana, Ofer
 586 Reiter, Cristina Carrera, Alicia Barreiro, Allan C Halpern, Susana Puig, et al. Bcn20000: Dermo-
 587 scopic lesions in the wild. *arXiv preprint arXiv:1908.02288*, 2019.
- 588 Li Deng. The mnist database of handwritten digit images for machine learning research. *IEEE
 589 Signal Processing Magazine*, 29(6):141–142, 2012.
- 591 Yukun Ding, Jinglan Liu, Jinjun Xiong, and Yiyu Shi. Revisiting the Evaluation of Uncertainty
 592 Estimation and Its Application to Explore Model Complexity-Uncertainty Trade-Off. In *2020
 593 IEEE CVPRW*, pp. 22–31, Seattle, WA, USA, June 2020. IEEE. ISBN 978-1-72819-360-1. doi:
 10.1109/CVPRW50498.2020.00010.

- 594 Carl Doersch. Tutorial on Variational Autoencoders, 2021. URL <http://arxiv.org/abs/1606.05908>.
- 595
- 596
- 597 Xiuyi Fan. Position paper: Integrating explainability and uncertainty estimation in medical AI. In
- 598 *Proceedings of the IEEE International Joint Conference on Neural Networks (IJCNN)*, 2025.
- 599 Yarin Gal and Zoubin Ghahramani. Dropout as a Bayesian Approximation: Representing Model
- 600 Uncertainty in Deep Learning. In *Proceedings of The 33rd ICML*, pp. 1050–1059, USA, June
- 601 2016. PMLR.
- 602
- 603 Muhammad Ghifary, W Bastiaan Kleijn, Mengjie Zhang, David Balduzzi, and Wen Li. Deep
- 604 reconstruction-classification networks for unsupervised domain adaptation. In *European con-*
- 605 *ference on computer vision*, pp. 597–613. Springer, 2016.
- 606 James Harrison, John Willes, and Jasper Snoek. Variational bayesian last layers. *arXiv preprint*
- 607 *arXiv:2404.11599*, 2024.
- 608
- 609 Kaiming He, Xiangyu Zhang, Shaoqing Ren, and Jian Sun. Deep residual learning for image recog-
- 610 nition, 2015. URL <https://arxiv.org/abs/1512.03385>.
- 611 James Hinns, Xiuyi Fan, Siyuan Liu, Veera Raghava Kovvuri, Mehmet Orcun Yalcin, and
- 612 Markus Roggenbach. An initial study of machine learning underspecification using feature at-
- 613 tribution explainable ai algorithms: A covid-19 virus transmission case study. In *PRICAI 2021:*
- 614 *Trends in Artificial Intelligence: 18th Pacific Rim International Conference on Artificial Intelli-*
- 615 *gence, PRICAI 2021, Hanoi, Vietnam, November 8–12, 2021, Proceedings, Part I 18*, pp. 323–
- 616 335, Vietnam, 2021. Springer.
- 617 Xinyue Hu, Zhibin Duan, Bo Chen, and Mingyuan Zhou. Enhancing uncertainty estimation and
- 618 interpretability via bayesian non-negative decision layer. *arXiv preprint arXiv:2505.22199*, 2025.
- 619
- 620 Eyke Hüllermeier and Willem Waegeman. Aleatoric and epistemic uncertainty in machine learning:
- 621 An introduction to concepts and methods. *Machine learning*, 110(3):457–506, 2021.
- 622 Pascal Iversen, Simon Witzke, Katharina Baum, and Bernhard Y. Renard. Identifying Drivers of
- 623 Predictive Aleatoric Uncertainty, 2024. URL <http://arxiv.org/abs/2312.07252>.
- 624
- 625 Laurent Valentin Jospin, Hamid Laga, Farid Boussaid, Wray Buntine, and Mohammed Bennamoun.
- 626 Hands-On Bayesian Neural Networks—A Tutorial for Deep Learning Users. *IEEE Compu-*
- 627 *tational Intelligence Magazine*, 17(2):29–48, May 2022. ISSN 1556-6048. doi: 10.1109/MCI.
- 628 2022.3155327.
- 629 Daniel S Kermany, Michael Goldbaum, Wenjia Cai, Carolina CS Valentim, Huiying Liang, Sally L
- 630 Baxter, Alex McKeown, Ge Yang, Xiaokang Wu, Fangbing Yan, et al. Identifying medical diag-
- 631 noses and treatable diseases by image-based deep learning. *cell*, 172(5):1122–1131, 2018.
- 632 Lennard Korte, Li Rong Wang, and Xiuyi Fan. Confidence estimation in analyzing intravascular
- 633 optical coherence tomography images with deep neural networks. In *2024 IEEE Conference on*
- 634 *Artificial Intelligence (CAI)*, pp. 358–364, Singapore, 2024. IEEE.
- 635
- 636 Veera Raghava Reddy Kovvuri, Hsuan Fu, Xiuyi Fan, and Monika Seisenberger. Fund performance
- 637 evaluation with explainable artificial intelligence. *Finance Research Letters*, 58:104419, 2023.
- 638 Mikhail Kulyabin, Aleksei Zhdanov, Anastasia Nikiforova, Andrey Stepichev, Anna Kuznetsova,
- 639 Mikhail Ronkin, Vasilii Borisov, Alexander Bogachev, Sergey Korotkikh, Paul A Constable, et al.
- 640 Octdl: Optical coherence tomography dataset for image-based deep learning methods. *Scientific*
- 641 *data*, 11(1):365, 2024.
- 642 Balaji Lakshminarayanan, Alexander Pritzel, and Charles Blundell. Simple and Scalable Predictive
- 643 Uncertainty Estimation using Deep Ensembles. In *Advances in Neural Information Processing*
- 644 *Systems*, volume 30, pp. 6402–6413, USA, 2017. Curran Associates, Inc.
- 645
- 646 Lei Le, Andrew Patterson, and Martha White. Supervised autoencoders: Improving generalization
- 647 performance with unsupervised regularizers. *Advances in neural information processing systems*,
- 31, 2018.

- 648 Peter K. Lee. *Actinic Keratosis, Basal, and Squamous Cell Carcinoma*, chapter 17. McGraw-Hill
 649 Education, New York, NY, 2017. URL accessmedicine.mhmedical.com/content.aspx?aid=1177005687.
 650
- 651 Scott Lundberg and Su-In Lee. A unified approach to interpreting model predictions, 2017. URL
 652 <https://arxiv.org/abs/1705.07874>.
 653
- 654 Andrey Malinin and Mark Gales. Predictive Uncertainty Estimation via Prior Net-
 655 works. In *Advances in Neural Information Processing Systems*, volume 31. Curran Asso-
 656 ciates, Inc., 2018. URL <https://proceedings.neurips.cc/paper/2018/hash/3ea2db50e62ceefceaf70a9d9a56a6f4-Abstract.html>.
 657
- 658 Lu Mi, Hao Wang, Yonglong Tian, Hao He, and Nir N. Shavit. Training-Free Uncertainty Estimation
 659 for Dense Regression: Sensitivity as a Surrogate. *Proceedings of AAAI*, 36(9):10042–10050,
 660 2022. ISSN 2374-3468. doi: 10.1609/aaai.v36i9.21243.
 661
- 662 Carlos Mougan and Dan Saattrup Nielsen. Monitoring Model Deterioration with Explainable Uncer-
 663 tainty Estimation via Non-parametric Bootstrap. *Proceedings of the AAAI Conference on Artifi-
 664 cial Intelligence*, 37(12):15037–15045, 2023. ISSN 2374-3468. doi: 10.1609/aaai.v37i12.26755.
 665 URL <https://ojs.aaai.org/index.php/AAAI/article/view/26755>.
 666
- 667 Mohammed Mustafa. Diabetes prediction dataset, version 1. <https://www.kaggle.com/datasets/iammustafatz/diabetes-prediction-dataset/data>, 2023.
 668
- 669 Stephen Odaibo. Tutorial: Deriving the Standard Variational Autoencoder (VAE) Loss Function,
 670 2019. URL <https://arxiv.org/abs/1907.08956>.
 671
- 672 Augustus Odena, Vincent Dumoulin, and Chris Olah. Deconvolution and checkerboard artifacts.
 673 *Distill*, 1(10):e3, 2016.
 674
- 675 Janis Postels, Hermann Blum, Cesar Cadena, Roland Siegwart, Luc Van Gool, and Federico
 676 Tombari. Quantifying aleatoric and epistemic uncertainty using density estimation in latent space.
 677 *CoRR*, abs/2012.03082, 2020. URL <https://arxiv.org/abs/2012.03082>.
 678
- 679 Janis Postels, Mattia Segù, Tao Sun, Luca Daniel Sieber, Luc Van Gool, Fisher Yu, and Federico
 680 Tombari. On the practicality of deterministic epistemic uncertainty. In Kamalika Chaudhuri,
 681 Stefanie Jegelka, Le Song, Csaba Szepesvári, Gang Niu, and Sivan Sabato (eds.), *International
 682 Conference on Machine Learning, ICML 2022, 17-23 July 2022, Baltimore, Maryland, USA*, vol-
 683 ume 162 of *Proceedings of Machine Learning Research*, pp. 17870–17909, USA, 2022. PMLR.
 684 URL <https://proceedings.mlr.press/v162/postels22a.html>.
 685
- 686 Murat Sensoy, Lance Kaplan, and Melih Kandemir. Evidential Deep Learning to Quantify Classifi-
 687 cation Uncertainty. In *Advances in Neural Information Processing Systems*, volume 31, Canada,
 688 2018. Curran Associates, Inc.
- 689 C. E. Shannon. A mathematical theory of communication. *The Bell System Technical Journal*, 27
 690 (3):379–423, 1948. ISSN 0005-8580. doi: 10.1002/j.1538-7305.1948.tb01338.x. URL <https://ieeexplore.ieee.org/abstract/document/6773024>.
 691
- 692 Jake Snell, Kevin Swersky, and Richard S. Zemel. Prototypical networks for few-shot learn-
 693 ing. In Isabelle Guyon, Ulrike von Luxburg, Samy Bengio, Hanna M. Wallach, Rob
 694 Fergus, S. V. N. Vishwanathan, and Roman Garnett (eds.), *Advances in Neural Infor-
 695 mation Processing Systems 30: Annual Conference on Neural Information Processing Systems
 696 2017, December 4-9, 2017, Long Beach, CA, USA*, pp. 4077–4087, USA, 2017. Curran
 697 Associates, Inc. URL <https://proceedings.neurips.cc/paper/2017/hash/cb8da6767461f2812ae4290eac7cbc42-Abstract.html>.
 698
- 699 Mukund Sundararajan, Ankur Taly, and Qiqi Yan. Axiomatic attribution for deep networks. In
 700 *International conference on machine learning*, pp. 3319–3328, Australia, 2017. PMLR.
 701

- Sing Yee Toh, Chang Cai, Li Rong Wang, Xiaoyin Bai, Joanne Ngeow, and Xiuyi Fan. The effect of explainable ai and uncertainty quantification on medical students' perspectives of decision-making ai: A cancer screening case study. In *Proceedings of the Extended Abstracts of the CHI Conference on Human Factors in Computing Systems*, CHI EA '25, New York, NY, USA, 2025. Association for Computing Machinery. ISBN 9798400713958. doi: 10.1145/3706599.3719791. URL <https://doi.org/10.1145/3706599.3719791>.
- Philipp Tschandl, Cliff Rosendahl, and Harald Kittler. The HAM10000 dataset, a large collection of multi-source dermatoscopic images of common pigmented skin lesions. *Scientific Data*, 5(1):180161, August 2018. ISSN 2052-4463. doi: 10.1038/sdata.2018.161.
- Dennis Ulmer, Christian Hardmeier, and Jes Frellsen. Prior and Posterior Networks: A Survey on Evidential Deep Learning Methods For Uncertainty Estimation. *Transactions on Machine Learning Research*, 2023, 2023.
- Uddesha Upadhyay, Shyamgopal Karthik, Yanbei Chen, Massimiliano Mancini, and Zeynep Akata. BayesCap: Bayesian Identity Cap for Calibrated Uncertainty in Frozen Neural Networks. In Shai Avidan, Gabriel Brostow, Moustapha Cissé, Giovanni Maria Farinella, and Tal Hassner (eds.), *Computer Vision – ECCV 2022*, pp. 299–317, Cham, 2022. Springer Nature Switzerland. ISBN 978-3-031-19775-8. doi: 10.1007/978-3-031-19775-8_18.
- Hanjing Wang, Bashirul Azam Biswas, and Qiang Ji. Optimization-Based Uncertainty Attribution Via Learning Informative Perturbations. In Aleš Leonardis, Elisa Ricci, Stefan Roth, Olga Russakovsky, Torsten Sattler, and Gü̈l Varol (eds.), *Computer Vision – ECCV 2024*, volume 15136, pp. 237–253. Springer Nature Switzerland, Switzerland, 2025. ISBN 978-3-031-73228-7 978-3-031-73229-4. doi: 10.1007/978-3-031-73229-4_14. URL https://link.springer.com/10.1007/978-3-031-73229-4_14.
- Li Rong Wang, Thomas C. Henderson, and Xiuyi Fan. An Uncertainty Estimation Model for Algorithmic Trading Agent. In Soon-Geul Lee, Jinung An, Nak Young Chong, Marcus Strand, and Joo H. Kim (eds.), *Intelligent Autonomous Systems 18*, pp. 459–465, Korea, 2024. Springer Nature Switzerland. ISBN 978-3-031-44981-9. doi: 10.1007/978-3-031-44981-9_39.
- Xiaosong Wang, Yifan Peng, Le Lu, Zhiyong Lu, Mohammad Bagheri, and Ronald M Summers. Chestx-ray8: Hospital-scale chest x-ray database and benchmarks on weakly-supervised classification and localization of common thorax diseases. In *Proceedings of the IEEE conference on computer vision and pattern recognition*, pp. 2097–2106, 2017.
- David Watson, Joshua O'Hara, Niek Tax, Richard Mudd, and Ido Guy. Explaining predictive uncertainty with information theoretic shapley values. *Advances in Neural Information Processing Systems*, 36:7330–7350, 2023.
- Claudius Zelenka, Andrea Göhring, Daniyal Kazempour, Maximilian Hünemörder, Lars Schmarje, and Peer Kröger. A simple and explainable method for uncertainty estimation using attribute prototype networks. In *Proceedings of the IEEE/CVF International Conference on Computer Vision*, pp. 4570–4579, 2023a.
- Claudius Zelenka, Andrea Göhring, Daniyal Kazempour, Maximilian Hünemörder, Lars Schmarje, and Peer Kröger. A Simple and Explainable Method for Uncertainty Estimation using Attribute Prototype Networks. In *2023 IEEE/CVF International Conference on Computer Vision Workshops (ICCVW)*, pp. 4572–4581, France, 2023b. IEEE. ISBN 979-8-3503-0744-3. doi: 10.1109/ICCVW60793.2023.00491. URL <https://ieeexplore.ieee.org/document/10350670/>.
- ## A APPENDIX
- ### A.1 DATASET DETAILS
- #### A.1.1 COVID-19 VIRUS TRANSMISSION DATASET
- (Hinns et al., 2021) is a tabular binary classification dataset comprising 3,553 instances. Each instance is characterized by 32 continuous features describing the United Kingdom's COVID-19 poli-

756 cies and daily case counts across 12 regions, covering the period from February 2020 to February
 757 2021. The dataset is labelled with a binary class indicating whether $R_t > 1$, where R_t represents the
 758 effective reproduction number. A value of $R_t > 1$ signifies an increasing spread of COVID-19. We
 759 randomly divided the dataset into three subsets: training (70%), validation (10%), and test (20%).
 760

761 A.1.2 DIABETES DIAGNOSIS DATASET

762 (Mustafa, 2023) is a tabular binary classification dataset comprising 100,000 instances, each repre-
 763 senting a patient. Each instance is described by eight features detailing the patient’s demographics
 764 (e.g., age and gender), pre-existing conditions (e.g., prevalence of heart disease), and vital signs
 765 (e.g., blood glucose level), and has a binary label indicating whether the patient suffers from dia-
 766 betes (0 indicating the patient is diabetes-free and 1 indicating the patient suffers from diabetes). We
 767 divided the dataset into three subsets for our experiments: training (80%), validation (10%), and test
 768 (10%).
 769

770 A.1.3 FUND PERFORMANCE EVALUATION DATASET

771 (Kovvuri et al., 2023) is a tabular binary classification dataset comprising 77,940 instances, designed
 772 to predict whether a fund’s net asset value (NAV) exceeds its NAV from the previous quarter. Each
 773 instance represents the state of one of 4,330 funds between March 2017 and June 2021, sampled
 774 quarterly. Each instance is characterized by 18 continuous features, including macroeconomic in-
 775 dicators (such as stock market returns (ST), exchange rate returns (EXR), and interest rates (IR)),
 776 country-level equity investment percentages and net asset data for the fund (covering 11 countries
 777 and “Other Country”), the Herfindahl–Hirschman index (HHI), and a past performance metric com-
 778 puted as the sum of class labels from the past four quarters (“L4f Gain”). We split the dataset into
 779 three subsets based on date: instances before March 2020 were assigned to the training set (66.7%),
 780 instances between March 2020 and June 2020 to the validation set (11.1%), and instances after June
 781 2020 to the test set (22.2%).
 782

783 A.1.4 ISIC

784 (Codella et al., 2019; Tschandl et al., 2018) is a dermoscopic image dataset containing instances from
 785 seven skin conditions: melanoma (MEL), melanocytic nevus (NV), basal cell carcinoma (BCC), ac-
 786 tinic keratosis (AKIEC), benign keratosis (BKL), dermatofibroma (DF), and vascular lesion (VASC).
 787 We followed the 2018 ISIC Challenge split, with 10,015 training, 193 validation, and 1,512 test im-
 788 ages. For the Out-of-Distribution (OOD) detection experiments, we constructed three OOD datasets
 789 with decreasing similarity to ISIC: (1) BCN-IN: 1,512 dermoscopic images of seen classes from the
 790 BCN20000 dataset (Combalia et al., 2019), (2) BCN-OUT: 313 images from the unseen class Scar,
 791 and (3) ChestMNIST: 1,512 images from the ChestMNIST dataset (Wang et al., 2017).
 792

793 A.1.5 OCTMNIST

794 (Kermany et al., 2018) is a retinal OCT image dataset comprising four classes: 47% Normal, 34%
 795 CNV (Choroidal Neovascularization), 11% DME (Diabetic Macular Edema), and 8% Drusen. We
 796 split the dataset into three subsets: 97,477 training, 10,832 validation, and 1,000 test instances. For
 797 the OOD detection experiments, we constructed three OOD datasets with decreasing similarity to
 798 OCTMNIST: (1) **OCTDL-IN**: 618 OCTDL (Kulyabin et al., 2024) images from seen classes, (2)
 799 **OCTDL-OUT**: 1,000 OCTDL images from unseen classes, and (3) **ChestMNIST**: 1,512 images
 800 from the ChestMNIST dataset (Wang et al., 2017).
 801

802 A.2 BASELINE DETAILS

803 We compared ReconstructionNet with recent state-of-the-art uncertainty estimates.

- 804
- 805 1. **Entropy** (Shannon, 1948) is derived from prediction probability.
 - 806 2. **Monte Carlo Dropout (MCD)** (Gal & Ghahramani, 2016) We apply dropout ($p = 0.5$)
 807 to the penultimate layer of the model and keep dropout active during inference to yield T
 808 predictions (where $T = 100$ for the Covid and Fund datasets, and $T = 10$ for all other
 809 datasets), following the hyperparameters in (Gal & Ghahramani, 2016).

- 810 3. **Deep Ensemble (DE)** (Lakshminarayanan et al., 2017) uses five models, with the standard
 811 deviation of their predictions as the uncertainty estimate.
 812
 813 4. **Posterior Network (PN)** (Charpentier et al., 2020) computes aleatoric uncertainty as the
 814 inverse of the maximum prediction probability and epistemic uncertainty as the inverse of
 815 the maximum of the Dirichlet distribution parameters.
 816
 817 5. **Bayesian Neural Networks (BNN)** (Jospin et al., 2022) estimate uncertainty as the stan-
 818 dard deviation of $T = 100$ predictions obtained with different weight samples.
 819
 820 6. **Evidential Deep Learning (EDL)** (Sensoy et al., 2018) estimates uncertainty using the
 821 entropy of the predicted probabilities.

821 A.3 METRIC DETAILS
 822

823 A.3.1 CORRELATION
 824

(Mi et al., 2022; Upadhyay et al., 2022) measures the reliability of the uncertainty estimate as the Pearson’s correlation coefficient between the uncertainty estimate and the prediction error (measured as the absolute difference between the one-hot label and the predicted probability). A higher correlation indicates a more reliable estimate, as prediction errors are likely to be high when the model’s uncertainty is high, and vice versa.

830 A.3.2 AURC (AREA UNDER RISK-COVERAGE CURVE)
 831

(Ding et al., 2020) quantifies the selectivity of the uncertainty estimate, indicating its usefulness in selective prediction i.e. making predictions only for confident instances. This is computed as the area under the risk-coverage curve, which plots the 0/1 loss (Risk) for instances with uncertainty scores within the α -percentile (Coverage) against the coverage. A selective uncertainty estimate would yield a low AURC, as it effectively reduces loss across all possible uncertainty thresholds.

837 A.3.3 SIGMA-RISK SCORE
 838

Evaluates the resilience of the uncertainty estimate to false negatives (incorrect instances with low uncertainty), which can lead to significant costs if many are left undetected. It is computed as the 0/1 loss of instances with normalized uncertainty less than $\sigma = \{0.1, 0.2, 0.3, 0.4\}$. A lower σ -risk score indicates greater robustness to false negatives. To ensure robustness to outliers, we apply min-max normalization with the minimum and maximum values computed after outlier removal with the interquartile range method.

846 A.3.4 OOD DETECTION
 847

(Lakshminarayanan et al., 2017; Postels et al., 2020; Malinin & Gales, 2018) Evaluates how effectively the uncertainty estimate can distinguish between in-distribution and OOD instances. This is quantified using AUROC (Area Under the Receiver Operating Characteristic Curve), where the true label indicates whether an instance is OOD and the target score is the uncertainty estimate. A higher AUROC reflects a more reliable uncertainty measure capable of identifying OOD inputs.

854 A.4 IMPLEMENTATION DETAILS
 855

The use of error weights ω allows the model to decouple the modeling of joint prediction probabilities from the classification task, enabling simultaneous optimization of both objectives. It also dynamically scales errors across classes to address variations in reconstruction difficulty and adjusts the contribution of each feature to the prediction, acknowledging that not all reconstruction errors equally impact the final outcome.

For image datasets, to reduce the size of the ReconstructionNet model, we trained class-specific decoders sharing a common encoder instead of training separate class-specific autoencoders. The encoder was based on a ResNet18 (He et al., 2015) backbone, and the decoders were implemented as inverted ResNet18 backbones, replacing convolutional layers with transposed convolutions.

Hyperparameters for all models were determined using grid search on the validation set. For ReconstructionNet, we tuned the compression ratio (which determines the latent vector length as its product with the feature count) along with the number of encoder and decoder layers, the width of intermediate layers, and the loss function parameter β ($\beta = 1.25, 2, 0.75$ for Covid, Diabetes, and Fund datasets). Both the MLP and ReconstructionNet models were trained on the training set with oversampling using SMOTE (Chawla et al., 2002). All models were trained using the Adam optimizer with early stopping. Each experiment was repeated five times, and we report the mean and standard deviation of each metric.

A.5 VERIFYING UNCERTAINTY EXPLANATION PROPERTIES WITH TOY EXAMPLES

A.5.1 IMPLEMENTATION INVARIANCE

We illustrate the property of implementation invariance with a simple example. Suppose we have two ReconstructionNet models, f and f' , that differ in architecture:

- f : Each class autoencoder is shallow and linear;
- f' : Each class autoencoder is deeper with nonlinearities.

If for every input \mathbf{x} , the two ReconstructionNet models yield identical prediction probabilities \hat{p} for all classes, then:

1. The predicted classes $c^* = \arg \max_j \hat{p}_j$ are identical,
2. The weighted reconstruction errors ϵ are identical,
3. The uncertainty explanations $\zeta(\mathbf{x})$, which are the feature-wise weighted reconstruction errors of the predicted classes, are identical.

Thus, ReconstructionNet's uncertainty explanations are *implementation-invariant* under this definition of functional equivalence.

A.5.2 SENSITIVITY

We illustrate the sensitivity property with a simple example. Consider a dataset where each input \mathbf{x} has three features, (x^1, x^2, x^3) . Suppose that for the predicted class c^* :

- The weighted reconstruction errors depend only on x^1 and x^2 ;
- The weight for x^3 is zero: $w_{c^*}^3 = 0$, indicating that changes in x^3 do not affect the class prediction.

The uncertainty explanation for input \mathbf{x} is given by:

$$\zeta(\mathbf{x}) = [w_{c^*}^1 \|x^1 - \hat{x}_{c^*}^1\|^2 \quad w_{c^*}^2 \|x^2 - \hat{x}_{c^*}^2\|^2 \quad w_{c^*}^3 \|x^3 - \hat{x}_{c^*}^3\|^2] \quad (15)$$

Since $w_{c^*}^3 = 0$, the explanation assigns zero attribution to x^3 , which is irrelevant to the prediction. Hence, ReconstructionNet's uncertainty explanations satisfy the *sensitivity* property: features irrelevant to the prediction receive zero attribution in the weighted reconstruction error.

A.5.3 CONSISTENCY

We illustrate the consistency property with a simple example. Consider an input $\mathbf{x} = (x^1, x^2, x^3)$; For the predicted class c^* , the uncertainty explanation is:

$$\zeta(\mathbf{x}) = [w_{c^*}^1 \|x^1 - \hat{x}_{c^*}^1\|^2 \quad w_{c^*}^2 \|x^2 - \hat{x}_{c^*}^2\|^2 \quad w_{c^*}^3 \|x^3 - \hat{x}_{c^*}^3\|^2] \quad (16)$$

Now consider a modification f' of the model f where feature x^2 is made more important for the prediction (i.e., its weight increases in the softmax over reconstruction errors).

- The reconstruction errors $\|x^j - \hat{x}_{c^*}^j\|^2$ remain unchanged, since the autoencoders are unchanged.
- The weight for x^2 increases: $w_{c^*}^{2'} > w_{c^*}^2$.

918 Then the uncertainty attribution for x_2 becomes:
 919
 920

$$\zeta(\mathbf{x})^2' = w_{c^*}^2 \|x_2 - \hat{x}_{c^*}^2\|^2 \geq w_{c^*}^2 \|x^2 - \hat{x}_{c^*}^2\|^2 = \zeta(\mathbf{x})^2. \quad (17)$$

921 Thus, increasing a feature’s contribution to the prediction does not decrease its uncertainty attribu-
 922 tion, demonstrating that ReconstructionNet’s uncertainty explanations satisfy the *consistency* prop-
 923 erty.

924 A.6 ADDITIONAL UNCERTAINTY EXPLANATION EXAMPLES

925 **MNIST:** The examples illustrate how the model’s uncertainty explanations correspond to ambiguous
 926 digit features that resemble other classes. In Figure 4a, the model predicted a 2 instead of a 0,
 927 showing uncertainty around the missing connection in the 0. In Figure 4b, it predicted a 6 instead of
 928 a 0, with uncertainty focused on the tail of the 6. In Figure 4c, the model again predicted a 6 instead
 929 of a 0, highlighting uncertainty on the right curve that resembles a 0. In Figure 4d, it predicted a
 930 9 instead of a 4, with uncertainty at the connecting bump of the 4 (which is atypical in a 9). In
 931 Figure 4e, the model predicted a 5, with uncertainty concentrated on the top tail of the digit. Finally,
 932 in Figure 4f, it predicted a 3 instead of an 8, highlighting the lower-left connecting curve, whose
 933 removal would make the digit resemble a 3 more strongly.

934 **ISIC:** The examples demonstrate how the model’s uncertainty explanations capture visual features
 935 that increase ambiguity in lesion classification, leading to misclassifications. In Figures 4g and 4h,
 936 the model misdiagnoses the dermoscopic image, with the uncertainty explanations highlighting a
 937 scab-like region. In Figures 4i, 4j and 4k, images were misclassified as MEL (melanoma) instead of
 938 BCC or AKIEC, with uncertainty concentrated on the uneven pigmentation of the lesion, a feature
 939 often associated with melanoma. In Figure 4l, the image was misclassified as AKIEC with uncer-
 940 tainty explanations highlighting the presence of hairs covering a substantial portion of the lesion.

941 **OCTMNIST** These cases illustrate how the model’s uncertainty highlights regions that contribute
 942 to misclassification in OCT images. In Figure 4m, the model classified the OCT image as DME,
 943 with uncertainty concentrated around one of the fluid pockets. In Figure 4n, the model predicted
 944 CNV instead of DME, again highlighting a fluid pocket. This reflects the ambiguity introduced by
 945 fluid pockets, which are common to both conditions. Figures 4o, 4p, 4q, and 4r are Drusen images
 946 misclassified as other conditions, with uncertainty explanations highlighting the deposits (uneven
 947 bumps in the OCT images), which are key features of Drusen and major contributors to the model’s
 948 uncertainty in each incorrect prediction.

949 A.7 COMPARISON WITH LLMs

950 Figure 5 compares uncertainty explanations from ReconstructionNet and a publicly available, off-
 951 the-shelf large language model (LLM; Microsoft Copilot). We observe that ReconstructionNet pro-
 952 duces more selective explanations, highlighting only small regions that contribute to uncertainty,
 953 whereas Copilot often highlights large areas (notably, in Figure 5b the entire digit is highlighted).
 954 Moreover, the regions identified by ReconstructionNet are more accurate. For example, in Figure 5a,
 955 where the digit 4 is misclassified as 7, ReconstructionNet correctly highlights the additional vertical
 956 line on the right, while Copilot highlights the connecting region that is common to both 4 and 7
 957 and should not confuse the model. Similarly, in Figure 5c, where a 6 is misclassified as 5, Recon-
 958 structionNet pinpoints the extra vertical line on the bottom left that distinguishes 5 from 6, whereas
 959 Copilot highlights the top-left vertical line, which can occur in both digits.

960 A.8 RELATION TO CONTRASTIVE LEARNING AND SIAMESE NETWORKS

961 Note that, although the training procedure of ReconstructionNet shares similarities with contrastive
 962 learning (Chopra et al., 2005), as both aim to minimize the distance between instances of the same
 963 class while maximizing the distance between instances of different classes, there are key differences
 964 in how these distances are computed. In contrastive learning, the distance is explicitly calculated
 965 as the L2-norm between the embeddings of a pair of instances. In ReconstructionNet, the dis-
 966 tance between an instance and the instances of a particular class is represented as the reconstruc-
 967 tion error of the corresponding class autoencoder. This distinction in distance measurement leads to
 968 differences in the training loss. While contrastive learning incorporates the L2-norm distance be-
 969 tween pairs of instances, ReconstructionNet uses class reconstruction error for its loss function.
 970

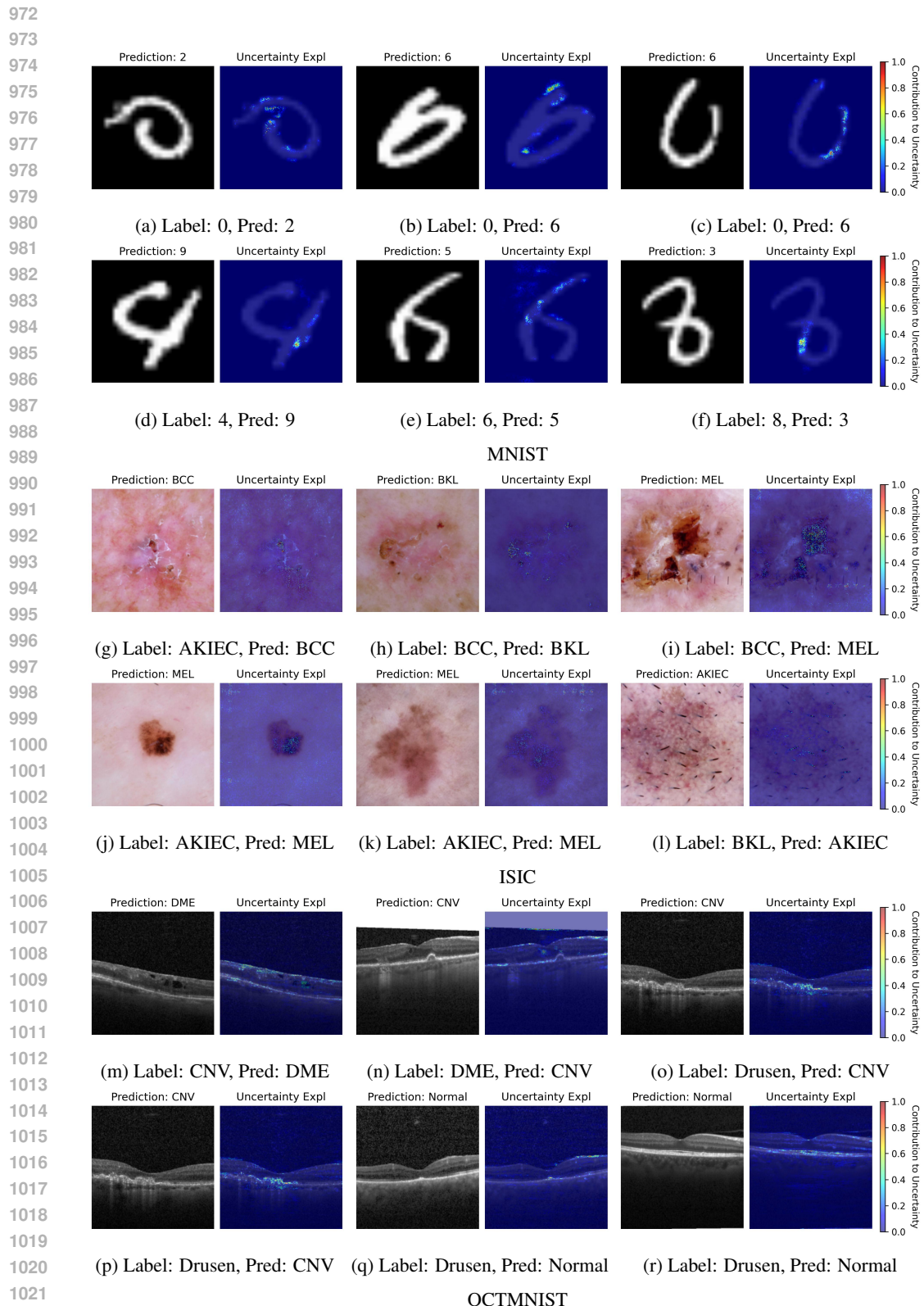
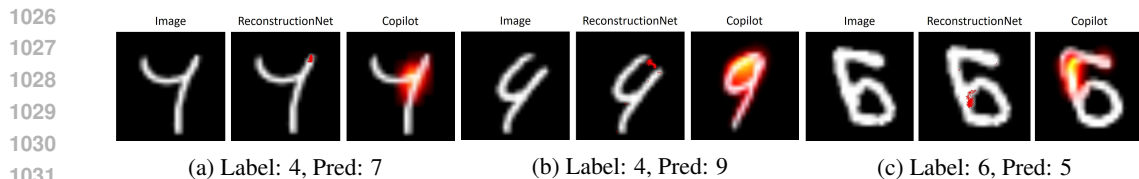


Figure 4: Uncertainty explanation illustration for MNIST, ISIC and OCTMNIST datasets. Positive uncertainty explanations were min-max normalized, gamma-corrected, and overlaid on the images for clarity. The highlighted regions “explain” the prediction uncertainty.



1032 Figure 5: Comparison of uncertainty explanations from ReconstructionNet and Microsoft Copilot
1033 on the MNIST dataset. Positive uncertainty explanations from ReconstructionNet were min–max
1034 normalized, with pixels having attribution greater than 0.2 shown in red and overlaid on the images
1035 for clarity. Microsoft Copilot explanations were generated using the prompt: “This image has been
1036 misclassified as [image class prediction]. Generate an image highlighting the regions contributing
1037 to prediction uncertainty in red.” The highlighted regions are intended to “explain” the prediction
1038 uncertainty.

1039 Furthermore, in contrastive learning, the distances between instances of different classes are ex-
1040 plicitly maximized and included in the loss function. In contrast, ReconstructionNet exclusively
1041 trains each class autoencoder with instances belonging to its specific class. The architecture of
1042 ReconstructionNet shares similarities with Siamese networks (Bromley et al., 1993) in its use of
1043 sub-networks. However, unlike Siamese networks, which share weights across sub-networks, Re-
1044 constructionNet allows each class autoencoder to have distinct weights.
1045

1046
1047
1048
1049
1050
1051
1052
1053
1054
1055
1056
1057
1058
1059
1060
1061
1062
1063
1064
1065
1066
1067
1068
1069
1070
1071
1072
1073
1074
1075
1076
1077
1078
1079